Excimer Laser Patterned Holey Graphene Oxide Films for Non-Enzymatic Electrochemical Sensing

Pratik Joshi[1,3], Shubhangi Shukla[2], Siddharth Gupta[3], Parand R. Riley[1], Jagdish Narayan[1,*], Roger Narayan[1,2*]

[1] Department of Materials Science and Engineering, North Carolina State University, Raleigh, NC 27695-7907, USA

[2]Joint Department of Biomedical Engineering, North Carolina State University, Raleigh, NC 27695-7907, USA

[3] Intel Corporation, Rolner Acres Campus 3, OR, 97124, USA

*Corresponding Author E-mail: narayan@ncsu.edu (Jagdish Narayan), rjnaraya@ncsu.edu (Roger Narayan)

Abstract:

The existence of point defects, holes, and corrugations (macroscopic defects) induce high catalytic potential in graphene and its derivatives. We report a systematic approach for microscopic and macroscopic defect density optimization in excimer laser-induced reduced graphene oxide (LIRGO) by varying the laser energy density and pulse number to achieve a record detection limit of 7.15 nM for peroxide sensing. A quantitative estimation of point defect densities was obtained using Raman spectroscopy and confirmed with electrochemical sensing measurements. Laser annealing (LA) at 0.6 Jcm^{-2} led to the formation of highly reduced GO by liquid phase regrowth of molten carbon with the presence of dangling bonds, making it catalytically active. Hall-effect measurements yielded mobility of ~200 $cm^2V^{-1}s^{-1}$. An additional increase in the number of pulses at 0.6 Jcm^{-2} resulted in deoxygenation through the solid-state route, leading to the formation of holey graphene structure. The average hole size showed a hierarchical increase, with the number of pulses characterized with multiple microscopy techniques, including SEM, AFM, and TEM. The exposure of edge sites due to high hole density after ten pulses supported the formation of proximal diffusion layers, which led to facile mass transfer and improvement in detection limit from 25.4 mM to 7.15 nM for peroxide sensing. However, LA at 1 Jcm^{-2} with 1 pulse, resulted in a high melt lifetime of molten carbon and the formation of GO characterized by a high resistivity of $3x10^{-2}$ Ω-cm, which was not ideal for sensing applications. The rapid thermal annealing technique using a batch furnace to generate holey graphene results in structure with uneven hole sizes. However, holey graphene formation using the laser annealing technique is scalable with better control over hole size and density. This study will pave the path for cost-efficient and high-performance holey graphene sensors for advanced sensing applications.

Keywords: Defect engineering, confocal Raman spectroscopy, electrocatalysis, melting, holey graphene

I. Introduction

Graphene and graphene derivatives have attracted significant interest for advanced sensing applications due to their high surface area to volume ratio. Reduced graphene oxide (rGO) exhibits high chemical stability, charge transport properties, and potential active sites, which are necessary for electrochemical sensing applications. The surface or interfacial defects present or introduced in rGO by fabrication or post synthesis are not detrimental for such applications as they serve as active sites for electrocatalytic reactions. The vacancy formation in graphene structure disrupts the σ and π bonding in carbon atoms located in the vicinity, leaving them under coordinated with dangling bonds, hence making the surface highly reactive[1]. In the case of Li-ion batteries, divacancies can act as sites for intercalation of Li ions[2]. Defects in graphene also act as sites for adsorption of gas molecules during gas sensing, making them efficient gas sensing materials. Dangling bonds in graphene can be introduced by a two-step process. The initial step involves the oxidation of graphene, leading to the formation of graphene oxide (GO). The presence of oxygen functionalization reduces the amount of sp^2 bonding, which degrades the electrical properties. The later step involves the reduction of GO to form rGO. This reduction introduces active carrier concentration and enhances mobility in these films. The thermal route for reduction of GO is not commercially viable as the conventional furnace-based thermal reduction of GO exposes the whole substrate to high temperatures, leading to electrode degradation. The chemical routes make use of highly toxic and hazardous chemicals; unwanted chemical impurities may adversely affect the catalytic properties[3].

Reduction of GO with laser is referred to as a 'green route' as it is environmentally safe. Studies comparing the properties of GO reduction using femtosecond, nanosecond (ns), and continuous-wave laser have shown that rGO obtained with ns laser pulses exhibits superior properties[4]. Notably, the non-equilibrium excimer laser-based GO reduction offers multiple advantages compared to the conventional reduction process. The adiabatic heat flow allows selective patterning of GO while maintaining the substrate at ambient temperatures. It has a high degree of spatial and temporal control with scale-up capabilities for wafer-scale integration[5]. In addition, the defect densities obtained in these films can be modulated by varying laser energy density, photon energy,

and the number of laser pulses. Laser reduction of GO is necessary for manufacturing supercapacitors, sensors, and transistors[6]. Previous works have shown the formation of micro-supercapacitor devices with good cyclic stability, and energy storage capacities of hydrated CO_2 laser reduced GO films[6]. The conversion of polymers to graphene by infrared laser was discovered in 2014 [7]. Researchers have reported the conversion of organic materials like wood, bread, potato, and coconut flakes to graphene with CO_2 laser[6]. Recently, the laser-based technique has been also utilized to synthesize bactericidal graphene coatings on face masks with advanced sensing capabilities[7]. Recent studies by Narayan et al. demonstrated the ability to melt carbon and Si-based materials by the laser annealing (LA) route with control over the penetration depth and undercooling [8,9]. Previous reports have shown the presence of ferromagnetism, p to n-type change in behavior, and high mobility in laser-induced rGO (LIRGO) films fabricated by liquid-phase regrowth of molten carbon under low undercooling conditions[10]. These properties arise due to the removal of the oxygen functional group, resulting in the occurrence of dangling bonds.

For superior electrochemical sensing, the use of holey graphene has gained traction. Moreover, the presence of holes results in enlargement of the contact between the electrode and the electrolyte, leading to shortening of the distance for ion/mass transport [11]. The exposed edges also improve the sensing performance owing to the fact that the electron distribution at the edge is different from that in basal plane; the free electrons at the edge are often localized and unpaired, making them chemically more reactive. Defects in rGO are also beneficial for sensitive and selective detection of various biologically significant chemicals such as methylxanthines, H_2O_2, and oxygen[12]. Hydrogen peroxide (H_2O_2) is the byproduct of several metabolic reactions in biological systems. In addition, it is closely related to cell proliferation, oxidative stress, physiological pathways in the human body; moreover, it often regulates the overall basal metabolic rate[13]. Its efficient quantitative estimation in body fluids and cell cultures can be a promising tool for the early detection of acute health problems. H_2O_2 levels are effective biomarkers for diagnosing cell death and cancer growth, cardiac aberrations, and genetic/somatic diseases linked to cerebral disorders (e.g., Alzheimer's disease and Parkinson's disease) [14–16]. Therefore, efficient methods for selective in vitro and in vivo sensing of H_2O_2 are required. Over the years, several sensing

techniques like electrochemical (e.g., cyclic voltammetry and linear sweep voltammetry), enzymatic, chemical and spectroscopy have demonstrated accurate evaluation of H_2O_2 levels. Compared to other approaches, voltammetric studies are observed to be more precise, explanatory, and cost-effective[17]. A few previous studies report a < 1 nM detection limit (LOD) for H_2O_2 sensing; non-enzymatic H_2O_2 sensing has demonstrated sensitivity in the micro – millimolar range[18 – 22].

Previous studies focused on holey graphene synthesis using CO_2 lasers (wavelength (λ) = 10,600 nm). The limit of resolution for the patterning process is directly proportional to wavelength of the laser that is used. Excimer lasers, which provide a smaller wavelength than other candidate lasers, possess the advantage of higher resolution, thus making the miniaturization and complex patterning process of LIRGO films feasible. This is the first study to report on the synthesis of holey graphene films using an ArF excimer laser (wavelength (λ) = 193 nm). In this study, we systematically evaluated the effect of laser energy density and the number of laser pulses on the formation of laser-induced rGO by utilizing these films for H_2O_2 electrochemical sensing. Further, we studied the variation of electron transfer kinetics as a function of film defect density. Finally, we demonstrated the applicability of this synthesis technique on flexible substrates for wearable sensing. The processing method described in this study has a high potential of technology transfer and scale up as the semiconductor industry is almost exclusively utilizing excimer lasers for patterning schemes.

II. Experimental

1) Pulsed laser deposition and laser annealing

The substrate utilized for this study was As-doped n-type <111> Si with a resistivity of ~0.005 Ω-cm, which was supplied by General Semiconductor (Hauppauge, NY). The a-C coatings were deposited on Si using pulsed laser deposition (PLD). Subsequently, laser annealing of the a-C coatings was performed using an ArF laser (λ =193 nm, 20 ns) with single and multiple pulses at an energy density in the range of 0.4–1.2 J/cm^2 at ambient temperature and pressure.

2) Instrumental methods

The electrochemical reduction was carried out on rGO films using the three-electrode configuration with an electrochemical workstation (Metrohm DropSense SPELEC, Oviedo, Spain). Raman studies were carried out using a 632 nm laser confocal micro-spectrometer (Horiba, Kyoto, Japan). The X-ray diffraction studies (XRD) were performed using a Rigaku Smart Lab X-ray diffractometer (The Woodlands, TX, USA) in Bragg-Brentano mode. The film microstructure was assessed by using a Verios 460L scanning electron microscope (FEI, Hillsboro, OR). The electrical behavior (Hall effect measurements) of a-C and r-GO films was studied using an HMS-3000 Hall measurement system (Ecopia, Anyang, South Korea). Details on the experimental parameters are provided in the ESI file.

III. Results and Discussion:

i. Fabrication and electrochemical study of LIRGO samples

(a) SEM study of fabricated rGO thin films

Fig. 2 (a) shows the SEM image of a-C thin film after laser irradiation at 0.4 Jcm^{-2}. It seems that the surface layer melted (appears bright in color) and formed rGO, whereas the bulk is still a-C, which appears dark in color. The rGO formed at this energy density is flat as well as free of ripples and wrinkles, as observed from the AFM surface scan (**Fig. S1 (a)**). The rGO formed at 0.4 Jcm^{-2} exhibited low roughness and an absence of ripples. The surface roughness for LIRGO at 0.4 Jcm^{-2} varied between 4-7 nm; the high flatness of rGO films formed at 0.4 Jcm^{-2} can be attributed to ultrafast melt quenching. Further, increasing the energy density to 0.6 Jcm^{-2} resulted in the formation of a rGO film with surface undulations (**Fig. 2(b)**). The Kikuchi pattern acquired from the liquid phase regrown rGO film is depicted in the **Fig. 2(b)** inset**.** The melt phase regrowth ensures *{0002}* epitaxial graphene on the *{111}* Si substrate. The high magnification image of LIRGO formed at 0.6 Jcm^{-2} confirmed the formation of ripples (**Fig. 2(c)**). Ripples may occur if the underlying a-C below rGO melts. Additionally, if the silicon substrate surface below the carbon film melts, then the silicon surface ripples can be incorporated into the graphene film, resulting in a graphene film with ripples. The melting of silicon under the oxide layer with a nanosecond pulse width laser has been verified previously[23]. For device-related applications,

the presence of ripples and wrinkles is undesirable as ripples and wrinkles contain numerous traps and defect centers and degrade the electrical characteristics. However, for electrochemical applications, the presence of corrugations (i.e., wrinkles, ripples, and crumples) increases the surface area of the sheet, resulting in better sensing efficiency. The higher surface roughness present at 0.6 Jcm^{-2} was further quantified using AFM (**Fig. S1 (b)**). The surface roughness varied between 30-50 nm.

Fig. 2(d) illustrates the structure after laser annealing at 0.6 Jcm^{-2} with 5 pulses. Notably, the structure shows the presence of nanoholes, which was not observed after 1 pulse. The formation of nanoholes is highlighted with yellow arrows. Interestingly, a higher hole density is observed along the ripples. The nanoholes can be formed by the coalescence of a large number of carbon vacancies, resulting in the enormous amount of dangling bonds needed for catalytic applications. The further increase in the number of pulses up to 10 (**Fig. 2(e)**) results in increase of hole size and density increase. The HRSEM image (**Fig. S2 (a)**) reveals an average hole size of 220±38 nm. The AFM (**Fig. S2 (b)**) also confirmed the formation of nanoholes. Further investigation of the AFM surface scan also revealed the presence of wrinkles. Wrinkles can result from the generation of thermal stress between the substrate and film during cooling. Studies have shown that topological defects like dislocation dipoles induce wrinkling. Finally, with 15 pulses the holes connect, resulting in film breakage. The film breakage exposed the substrate and *<111>* Si substrate; the corresponding Kikuchi pattern from the substrate is depicted in an inset to the **Fig. 2(f)** inset. **Fig. S3** shows the SEM micrograph after laser annealing at 1 Jcm^{-2}, revealing a further rise in wrinkle and ripple density as compared to that from irradiation at 0.6 Jcm^{-2}. The SEM results suggest the possibility of excellent electrochemical properties due to defects in these films.

(b) Electrochemical behavior of LIRGO films fabricated using varying laser parameters

We aimed to investigate the response of laser-induced rGO films towards electrochemical H_2O_2 reduction via the cyclic voltammetry (CV) technique. The LIRGO films produced under variable energy densities and laser pulse conditions were used as probes for voltammetric H_2O_2 sensing. Before electrocatalysis, the stability and reversible behavior of modified electrodes were studied against ferricyanide redox species as shown in **Fig. S4**. The overall reaction for H_2O_2 reduction is:

$$H_2O_2 \rightarrow H_2O + 1/2\,O_2 \quad (1)$$

The LIRGO electrode fabricated at energy densities 0.4, 0.6, and 1.0 Jcm^{-2} are referred to as $E_{0.4}$, $E_{0.6}$, $E_{1.0}$. **Fig S5** and **Fig. 3** depict the voltammograms of rGO coated Si electrodes in 0.5 M PBS (pH 7.2) containing 0.1 M KCl over serially diluted concentrations of H_2O_2 (0.21 nM – 65 mM) at a scan rate of 30 mV s^{-1} within the potential window of 0.3 – -0.8 V. The CV curve for the electrode $E_{0.4}$ did not show a significant electrochemical response towards the reduction of H_2O_2 over the entire range, except a feeble increase in the cathodic current of ~ 0.35 µA at higher concentrations (1.8 mM) (**Fig S5a – b**). However, an apparent non–linear increase in peak current was observed along with the forward scan for higher concentrations. The low current may be attributed to mere surface melting when annealed at 0.4 Jcm^{-2} (as observed from SEM imaging) (**Fig. 2(a)**). The electrode $E_{0.6}$ demonstrated a peak current of ~ 1.2 µA on successive addition of H_2O_2 solution. Equivalent amplification in the current responses was recorded at -0.1 V, upon individual addition of 0.20 nM – 60 mM H_2O_2 concentrations as shown in **Fig. 3a**. The calibration plot of peak current versus concentration evidenced a relatively broad linear detection spectrum from µM to several mM (**Fig. 3i**). The high detection limit achieved may be due to the surface undulations in the rGO film as discussed under microscopic characterization (SEM).

The CV responses on electrode $E_{1.0}$ also showed an increase in the reduction current after the subsequent addition of H_2O_2 solutions (**Fig. 3b**). Here, the increase in the faradic current for the reverse sweep was less proportional to the H_2O_2 concentration and lower, as evident from the corresponding calibration plot **(Fig. 3ii inset)**. The limit of detection for this $E_{1.0}$ was around 1.7 mM, which is ~100x higher than the electrode $E_{0.6}$. Additionally, the sensitivities of 0.1943 ± .006 µA mM^{-1}, 0.1534 ± 0.014 µA mM^{-1} were recorded for $E_{0.6}$, $E_{1.0}$ electrode films. The catalytic sensitivities and LOD obtained for these films are summarized in **Table 1**.

Considering the significant results obtained for electrochemical reduction with the electrode $E_{0.6}$, the effect of the number of laser pulses at 0.6 J cm^{-2} was investigated. **Fig. 3 (a, c, and d)** shows the voltammograms recorded on rGO films deposited with an increasing number of laser pulses (1, 5, and 10). The polarization curves recorded for different electrodes (referred to as $E_{1\ pulse}$, $E_{5\ pulse}$, and $E_{10\ pulse}$) showed remarkable

differences in electrochemical behavior towards H_2O_2 reduction as evident from **Fig. 3c-d.** The typical voltammetric response on $E_{1\ pulse}$ showed a significant increase in cathodic current (around 1.2 µA) at a potential value of ~ 0.15 V upon injecting successive H_2O_2 concentrations from 0.21 nM – 60 mM. For $E_{5\ pulse}$ and $E_{10\ pulse}$, current amplification was higher as compared to that monitored on $E_{1\ pulse}$. Along with the improvement in current signals, dynamic shifts in potential were also observed; $E_{5\ pulse}$ showed a noticeable gradual deviation from -0.14 V to a relatively lower potential of -0.11 V, while E_{10} exhibited a more detectible transition to an even lower potential of -0.9 V on the subsequent addition of H_2O_2. Further, the corresponding calibration plots (**Fig. 3 (i, iii, iv)**) yield the limit of detection for electrode films E_1, E_5 and E_{10} as 25.4 µM, 1.2 µM, and 7.15 nM. The sensitivities of differently modified electrodes ($E_{1\ pulse}$, $E_{5\ pulse}$, $E_{10\ pulse}$) were estimated as 0.1943, 0.202, and 0.2353 mA M^{-1} cm^{-2}, respectively [24]. Electrode E_{10} shows a higher sensitivity as well as detection limit in comparison to $E_{5\ pulse}$ and $E_{1\ pulse}$.

Further, voltammograms were recorded on the electrodes $E_{1\ pulse}$, $E_{5\ pulse}$, and $E_{10\ pulse}$ at different scan rates (2 to 300 mV/s) using 1.8 mM H_2O_2 in 0.1 M PBS solution to analyze the role of surface or diffusion processes in the propagation of reaction kinetics. **Fig. 4** shows the increments in cathodic peak currents for E_{10} increased linearly with the advancing scan rates as evident from **Fig. 4a**, while the rest of the electrodes ($E_{1\ pulse}$ and $E_{5\ pulse}$) had a much lower current response and did not exhibit any direct correlation with different scan rates (**Fig. S6**). Based on the slope for $E_{10\ pulse}$ (shown in **Fig. 4b)**, the diffusion coefficient of H_2O_2 was calculated as 1.71 x 10^{-4} cm^2 /s using the Randles-Sevcik equation (eq. 3). For $E_{1\ pulse}$ and $E_{5\ pulse}$, the values were very low due to non-linear and relatively less steep calibration curves. Thus, the electrochemical reduction process was observed to be diffusion controlled in liquid for $E_{10\ pulse}$, whereas $E_{1\ pulse}$ and $E_{5\ pulse}$ exhibited surface-controlled electrode kinetics.

$$Ip = 2.69 \times 10^5\, n_2^3\, AD\, \tfrac{1}{2}\, Cv_2^1 \qquad (3)$$

ii. Defect and structural characterization

The Raman, AFM, TEM, XRD, XPS, and Hall effect measurements were performed to get further insight into the effect of defect chemistry on the electrochemical sensing behavior in the synthesized rGO samples.

(a) Raman spectroscopy

Graphene and its derivatives exhibit well-known Raman signature peaks. Defect-free graphene and graphite exhibit a sharp G peak at ~1570 cm^{-1} with the presence of weak or no D peak (**Fig. 5 (a)**) [25]. The D peak arises due to a combination of disordered regions and point defects centered at ~1350 cm^{-1} [26]. The D peak intensity rises with increasing point defect concentration. Studies have also demonstrated the appearance of the D' peak at higher defect concentrations. The D' peak occurs at 1620 cm^{-1}. The proton beam irradiated graphene also exhibits unique f peaks centered at 1450 and 1560 cm^{-1} [27]. At higher wavenumbers, graphene exhibits a 2D peak at 2740 cm^{-1}, D+G peak at 2940 cm^{-1}, D+D', and 2D' breathing modes [28].

Fig. 5 (a, b) shows the Raman spectra of laser irradiated a-C films at varying energy densities from 0.4- 1.0 Jcm-2. The spectra were normalized with respect to the intensity of the G peak for the sake of comparison. Laser annealing a-C at 0.4 Jcm^{-2} (**Fig 5(a)**) yields a noticeable change in the Raman spectrum compared to pristine a-C **(Fig. 5(c))**. The peak fitting was carried out based on the above-discussed formalism. The G peak for a-C that was laser annealed at 0.4 Jcm^{-2} was centered at 1575 cm^{-1} (very close to the G peak of graphite), which indicates the formation of sp^2 crystalline regions after laser annealing. The a-C films annealed at energy density $\geq$0.6 Jcm-2 showed a significant blue shift compared to the equilibrium graphitic G peak position. The stress buildup in these films can be estimated as 4.1cm-1/GPa [29]. This value signifies the abundance of defects in the films irradiated at high energy density, which are ideal for electrocatalytic applications. The Raman spectra of rGO films synthesized at different energy densities have been fitted to the D4 peak (~1200 cm^{-1}), D peak (1360 cm^{-1}), D" (1500 cm^{-1}), G peak (1580-1600 cm^{-1}), and D' peak (1620-1630 cm^{-1}) as shown in **Fig S7**. Laser annealing at 0.6 Jcm^{-2} results in an increased I_d/I_g ratio as compared to 0.4 Jcm^{-2}, suggestive of more reduction in these films. The increased I_d/I_g ratio reflects an increased number of sp^2 domains with reduced cluster size in the structure. The films obtained at 0.6 Jcm^{-2} are more reduced as compared to the films obtained

at 0.4 Jcm^{-2}; only surface melting occurs at 0.4 Jcm^{-2}, resulting in an incomplete reduction. The higher degree of reduction with increased I_d/I_g ratio is in agreement with previously reported studies [30, 31]. The films annealed at 0.6 Jcm-2 also show sharp 2D, D+G, and 2D'+G peaks. The presence of a 2D' peak visible after LA at 0.4 Jcm^{-2} may be a result of sp^3 bonded carbon present beneath the melted layer. The I_d/I_g ratio increases further with the increase in the number of laser pulses at 0.6 Jcm^{-2}, indicative of significant reduction. **Table 2** depicts the increase in the Id/Ig ratio at 0.6 Jcm^{-2} with an increasing number of pulses. Notably, the presence of a 2D' peak after 10 pulses at 0.6 Jcm^{-2} indicates the formation of a high amount of disorder in these films, which is due to surplus carbon vacancy formation that coalesces to form nanoholes.

Cancado et al.[32] performed a detailed study to quantify the defects in graphene induced by Ar ion irradiation using Raman spectroscopy and demonstrated that the I_d/I_g ratio of graphene films varies with the distance between the defects, L_D. Interestingly, the maximum attainable I_d/I_g ratio varies with the Raman excitation wavelength used to perform the study. Specifically, I_d/I_g refers to the ratio of the area of D peak to that of G peak. Defect formation in graphene occurs in three stages. Initially in stage I, the I_d/I_g ratio increases with increasing defect density until it reaches a high point where the structure is termed as nanocrystalline graphene due to the formation of nanodomains[33], afterwards in stage II, the I_d/I_g ratio starts to decrease with increasing defects. Here, the graphene structure starts to collapse, and oxygen starts entering into the lattice. Finally in stage 3, the I_d/I_g approaches zero, and the structure is completely amorphized. In this study, the I_d/I_g ratio was ~1 for 0.4 Jcm^{-2} annealed sample and increased to 2.5 at 0.6 Jcm^{-2}. However, the ratio started to decrease after annealing at energy densities >0.6 Jcm^{-2}, indicating the onset of stage II and the formation of graphene oxide. This trend is demonstrated in **Fig. S8**.

The Tuinstra–Koenig (T_K) relation is used to estimate the relative number of defects in the graphene film. In stage I, the nano-crystallite size (La) along the graphene basal plane is given by:

$$L_a = (2.4*10^{-10})*\lambda^4*(I_d/I_g)^{-1} \quad (4)$$

where λ is the wavelength of the Raman laser used for excitation.

Defect density in graphene is given by:

$$n_D = \frac{2.4*10^{22}}{\lambda^4}\frac{I_D}{I_G} \quad (5)$$

The quantitative measurements obtained from Raman analysis have been summarized in **Table 2**.

(b) X-ray Diffraction (XRD) and X-ray Photoelectron Spectroscopy (XPS)

The XRD results from the as-deposited a-C thin film and LIRGO synthesized at varying laser annealing energy densities are shown in **Fig 6(a)**. The broad a-C peak was found to be centered at ~14.5°, indicative of a loosely packed structure. A peak at 25.58° appears after laser annealing a-C at 0.4 Jcm^{-2}, illustrating the formation of rGO by liquid phase regrowth of molten carbon with the presence of an a-C peak. The presence of an a-C peak further confirms the fact that only surface melting occurred. The FWHM of the rGO peak was calculated to be 0.1298. The observed (002) peak corresponds to an interlayer distance of 0.35 nm. By utilizing the Scherer equation (L (nm) = 0.1386/β$\cos\theta$), the average crystallite size of the rGO formed by liquid-phase regrowth of molten carbon was calculated to be around 65.58 nm. This value is twice that obtained from Raman measurements and indicates the possibility of different crystallite sizes in the center and edge of the sample, possibly due to higher cooling rates at the edges as compared to the center. The large crystallite size shows the possibility of the use of LIRGO formed at 0.4 Jcm^{-2} for solid-state devices. After laser annealing at 1 Jcm^{-2}, the peak at 25.58° left shifts to 20.5°, which is attributed to oxygen incorporation in the rGO interlayers that leads to expansion along the c-axis. By utilizing the Scherer equation, the crystallite size was calculated to be around 56 nm. The excimer laser-induced rGO is formed by liquid-phase regrowth of a-C resulting in closed packed structure along the basal plane compared to rGO synthesized by chemical routes. The XRD of rGO reported is consistent with previous studies on rGO synthesized by non-equilibrium flash joule heating, excimer laser, and microwave radiation[10,33–35].

The mechanism of direct laser writing of rGO onto GO films involves photoreduction and thermally assisted structural rearrangement [4]. The XPS fitting of the C-1s peak for LIRGO synthesized at 0.6 Jcm^{-2} is depicted in **Fig. 6(b)**. The Gaussian fitting was performed by considering C-C (sp^2), C-C (sp^3), C-OH, C-O-C, and C=O

bonds at 284.5, 285.1, 285.7, 286.7, and 288 eV, respectively. The sp^2/sp^3 ratio was determined to be 0.7. The empirical equation reported for computing the C/O ratio for rGO based materials from XPS is [36]:

$$\frac{O}{C} = \frac{A_{C-OH} + A_{C=O} + 0.5\,A_{C-O-C}}{A_{total}} \quad (6)$$

The C/O ratio was calculated to be 5.2 for LIRGO synthesized at 0.6 Jcm^{-2}. The C/O ratio after multiple laser pulses was not quantifiable as the presence of nano and microholes resulted in stray signals from the Si substrate and the oxide present on top of it.

(c) Hall Effect

Fig.7 (a) portrays the majority charge carrier concentration of a-C films annealed at different laser annealing energy densities. The electron carrier concentration is at a maximum at 0.4 Jcm^{-2} (~ $-1x10^{-21}$ $/cm^3$). Interestingly, laser annealing at 0.4 Jcm^{-2} results in n-type conductivity; however, a-C has p-type conductivity. As evidenced from SEM and Raman characterization, after laser annealing at 0.4 Jcm^{-2}, there is only surface melting. The relation $\sigma = ne\mu$ has to be satisfied, where σ is the electrical conductivity, n is the concentration of free electrons, and μ is the electron mobility. The high values of n and σ suggest low mobility, which perhaps is due to incomplete melting. At 0.6 Jcm^{-2}, the LIRGO film shows a slightly lower charge carrier concentration than 0.4 Jcm^{-2}; it is still high compared to the a-C film, which exhibited a carrier concentration of $10^{-15}/cm^3$. The recorded mobility values were low (~ 200 $\frac{cm^2}{Vs}$).

The low mobility values can be explained from the observations associated with SEM analysis; the films at 0.6 Jcm^{-2} showed the presence of defects such as ripples and wrinkles. These defects are not ideal for electron mobility as these defects act as traps and scattering centers for free electrons, limiting the mobility of electrons. At 0.8 Jcm^{-2}, a further drop in the electron carrier concentration and mobility was recorded compared to those recorded for the 0.6 Jcm^{-2} films. From the XRD analysis, at higher laser energy densities, oxygen starts entering the interlayers, leading to structure expansion. The Raman analysis also indicated the start of GO formation. Hence, the observed decrease in values can be attributed to higher defect scattering in the structure along with increased wrinkling and rippling. Raman spectroscopy showed a high reduction of films at 0.6 Jcm^{-2}. The

reduction of GO occurs by the removal of the oxygen functional group. The removal of oxygen can result in a dangling bond. If the presence of oxygen is considered as a lattice site, then the removal of oxygen present in the a-C film can generate 2 electrons for conduction as depicted in equation (7):

$O_o \leftrightarrow \ddot{V_o} + 0.5O_2 + 2e'$; $K_1 = [\ddot{V_o}]e'^2 P_{O2}^{0.5}$ (7)

Due to high reduction at 0.6 Jcm^{-2}, optimized values of mobility, resistivity, and carrier concentration were achieved even though the structure showed the presence of ripples (**Fig. 7(b)**).

Further, the effect of number of laser pulses at 0.6 Jcm^{-2} on the electrical behavior of fabricated films was investigated as shown in **Fig 7(c, d)**. Notably, the mobility decreased with an increase in the number of pulses. However, there is not a significant drop in conductivity, suggesting an increase in carrier concentration with the number of pulses. The increase in carrier concentration can be understood if the rGO film has surplus dangling bonds. The SEM study indicated the formation of nano and microholes, whereas the Raman study indicated higher reduction with increased pulses. This result suggests the removal of the oxygen functional group as well as the formation of carbon vacancies, coalescing to form nanoholes. Both carbon vacancies and/or removal of the oxygen functional group lead to the presence of dangling bonds. Yet, there is significant deterioration in mobility due to holes and wrinkles that cannot be neglected. The film mobility dropped to ~100 $\frac{cm^2}{Vs}$ after 10 pulses. However, this situation is ideal for electrocatalytic applications as the drop in mobility is compensated by the high active carrier concentration necessary for high reactivity. The Hall effect measurements were not carried out after 15 pulses as we observed significant film degradation. The exact values of mobility and resistivity are tabulated in **Table 3**.

(d) AFM and TEM

The 2D AFM surface scan of rGO fabricated at 0.6 Jcm^{-2} after 5 laser pulses is depicted in **Fig. 8(a)**. The presence of wrinkles, ripples, and microholes is evident. The formation of disclination and dislocations in the structure induces wrinkling[37]. The presence of holes is highlighted with black arrows. The average size of the microholes was 150±40 nm. Interestingly, the majority of microholes formed were observed on the hillocks.

Simulation studies [46] have shown that the hillock regions of ripples in graphene are highly strained, making bond breaking and vacancy coalescence in such regions easier.

Previous studies have indicated the high crystalline nature of the rGO films obtained by laser annealing at 0.6 Jcm^{-2} pulse. The synthesized rGO exhibited a sharp SAED spot pattern along the $[4\bar{2}\bar{2}\bar{3}]$ zone axis without the presence of any vacancies[10]. The formation energy of a mono-vacancy in graphene is very high (~8eV), whereas di- and multivacancy formation are thermodynamically more favorable yet not feasible with 1 pulse of energy from the ArF laser. However, multiphoton absorption can lead to multivacancy generation. This can be achieved by irradiating rGO with multiple pulses. **Fig. 8(b)** is a low magnification image of the rGO flake formed after irradiation at 0.6 Jcm^{-2} with 3 pulses, which was collected on the sample grid after ultra-sonication for TEM structural investigation. **Fig. 8(c)** illustrates the HRTEM micrograph of LIRGO obtained at 0.6 Jcm^{-2}-3 pulses. The image demonstrates a combination of strong (dark), grey, and bright contrast areas on the sheets at 5 nm scale, possibility due to the presence of monolayer to multilayered regions as previously observed by Mayer et al[38]. Perhaps the brighter-looking regions may also represent the ripple formations in the sheet. The presence of many dark circular-looking spots represents nano-holes. The inset (green box) shows a high magnification image of one such nanohole. The average nanohole size observed was 2.0±0.5 nm. The inset (red box) indicates the presence of carbon atoms with a pure hexagonal orientation matching up with graphite atomic spacing values. **Fig. 8(d)** illustrates the FFT of the multi-layer rGO exhibiting hexagonal pattern[38]. The amount of disorder within the structure was higher as compared to that after 1 pulse. From the FFT, the average measured distance from the center to the first observed spot is ~4.7 nm^{-1}; the further away spot measures 8.13 nm^{-1}, which is consistent with the standard graphene FFT pattern.

iii. Structure-property correlation

The structural characterization revealed that the LIRGO films fabricated with variable energy densities have vast structural differences such as the absence or presence of ripples, wrinkles, oxygen in the interlayers, holes, and sp^2 clusters. Therefore, the obtained results provide a gateway for systematic defect modulation in these films. An energy density <0.4 Jcm^{-2} is not sufficient for melting of a-C films as evidenced experimentally. The

surface melting threshold for a-C on a Si substrate can be calculated using the equation $E_{th} = \frac{K\Delta T \tau^{0.5}}{(1-R_L)D^{0.5}}$ Here, ΔT denotes the difference between the substrate temperature and melting temperature of amorphous carbon, R_L denotes the reflectivity of the amorphous carbon (=0.3), and D is the diffusivity of amorphous carbon at room temperature[39]. E_{th} was calculated to be 0.42 Jcm^{-2}. Laser annealing at 0.6 Jcm^{-2} led to the formation of highly crystalline rGO, with a sharp XRD peak at 25.5°. In comparison, the XRD peak obtained after chemical reduction using a sodium-ammonia solution was broad and centered at 23°, suggesting the structure was not fully closed pack (possibly due to the presence of surface functional groups) [40]. The LIRGO at 0.6 Jcm^{-2} also shows the presence of surface corrugations. Macdonald et al. [41,42] demonstrated the direct relationship between nanoscale irregularity/roughness of the electrode with non-faradic as well as capacitive current variations in the double layer. Here, the asymmetric surface topology contributes to enhancement in the real as well as the geometric surface area of the electrode, which is eventually responsible for non-ideality in charge transfer effects and diffusion at the electrode/electrolyte interface. In this study, the C/O ratio of rGO achieved was ~5, demonstrating the moderate reduction achieved in these films. Previous studies have demonstrated that the C/O ratio in GO reduced by ArF excimer laser can be varied from 3.8 to 15.6 [10]. This finding suggested the need for multiple pulses intended for further reduction. The reduced GO films obtained in this study have comparable Raman with those recently reported in the literature. However, it is important to note that the good sensing behavior of GO films in current study is due to high reduction as well as the presence of holes in the film.

Multiple pulses at 0.6 Jcm^{-2} resulted in the formation of nano and microholes. The holes are formed due to the deoxygenation process, resulting in higher reduction[52]. A similar structure has also been observed by Lima et al.[53] after laser reduction of GO by a 1064 nm laser. The higher deoxygenation signifies a higher amount of reduction in these films. The formation of holes also suggests solid-state reduction after 5 pulses. This result can be explained by rGO formation after 1 pulse by liquid phase regrowth of molten carbon with very high electrical and thermal conductivity. Hence, the successive shots are unable to melt the formed rGO, and reduction proceeds through the solid-state route. This result also explains the increase in wrinkling observed

after an increasing number of laser pulses at 0.6 Jcm^{-2}. The regions with holes expose the highly reactive edge sites. The surface and edge defects in nanomaterials are recognized as highly active and unstable centers since they are comprised of uncoordinated valences or reactive dangling bonds, which regulate the electrocatalytic properties. With the increasing number of pulses (~10), the hole density increases, reaching a maximum value after which the film starts tearing apart. The detailed laser-solid interaction simulations of these transformations have been reported previously[45].

The laser annealing at a higher energy density of 1 Jcm^{-2} also induced surface undulations in the rGO structure, confirming the formation of rGO by liquid phase regrowth of molten carbon. However, the high melt lifetime leads to high film stress as well as films with low conductivity and mobility due to oxygen creeping into the loosely packed structure as characterized by XRD and Hall effect measurements. The rGO films synthesized at 1 Jcm^{-2} exhibit a high surface area; the electrical properties are below the required values, disrupting the stability of current flow and thus showing suboptimal efficiency. Further, the effective electrochemical surface area (ECSA) for $E_{10\ pulse}$ electrode was obtained as 0.01133 cm^{-2} using Equations 8 and 9, which was the highest among the films (details in ESI file).

$$ECSA = Cdl/Cs \quad (8)$$

$$Cs = A/2km\Delta V \quad (9)$$

Moreover, the optimal electrochemical activity was achieved by balancing the defect density and conductivity. It has been demonstrated in previous reports that increasing the defect density can lead to a higher density of states, which leads to faster kinetics. We calculated the charge transfer kinetics using the equation:

$$k^0 = 2.18(\alpha nFD/RT)^{1/2} e^{-[(\alpha^2 F/RT)\, n\Delta E_P]} \quad (10)$$

On comparing the defect densities recorded from the Raman studies, it is observed that the rate constants are directly proportional to the number of defects. Therefore, the LIRGO film with greater defect density showed faster electrochemical kinetics.

Hydrogen peroxide undergoes reduction when it comes in contact with defects that are present in rGO film. Notably, the defects present in these films have a high localized electron concentration. The defects such as holes and wrinkles also provide a higher surface contact area which leads to a shortening of the distance for ion/mass transport further facilitating the reduction of H_2O_2. The active surface area termed electroactive contact surface area (ECSA) and the charge transfer kinetics calculations shown above are in agreement with the above-discussed mechanism. It is interesting to note that if the GO is not completely reduced, it has higher oxygen content present on defect sites then there is a possibility of oxygen transfer from GO to H_2O_2 resulting in oxidation rather than reduction of H_2O_2. The less reduced graphene films at 0.4 Jcm^{-2} exhibited a remarkable rise in anodic current at higher potential was obtained along with feeble cathodic component, due to oxidation of H_2O_2 by consuming available oxygen from the GO.

iv. Significance of results obtained

Rapid thermal annealing (RTA) using a batch furnace is a well-established method for holey graphene synthesis. In this method, the temperature of the furnace is ramped at a high rate for reduction of GO. The reduction results in CO_2 gas liberation, which is liberated by piercing of the surface and the formation of holes[48,49]. This method needs significant efforts for control of the hole size and density as the hole size range is too large (10-250 nm). However, holey graphene formation using the laser annealing technique is scalable with tunable hole size and density. Furthermore, the defect modulation in graphene with excimer laser irradiation is a topic of significant research for catalysis applications. Recently, the defects induced in graphene formed on the surface of SiC upon irradiating SiC with an ArF laser (6.5 eV photon energy) were studied using conductive AFM surface maps[50]. The study observed the formation of carbon vacancies in these films after multiple laser pulses and various other defects including Stone–Wales defects[50]. The current study verifies the formation of carbon vacancies after multiple laser pulses. Further, the observation of the preferential formation of vacancies and holes on ripples and wrinkles in this study will have significant implications on the control of hole densities for electrocatalysis applications.

This is the first work to report the electrochemical properties of a-C film reduced with an ArF laser. One of the previous studies focused on the fabrication of highly porous graphene from Bakelite polymer with 1064 nm laser energy for use as electrodes in supercapacitors[51,52]. The exceptional properties observed were attributed to the nanosecond pulse width of the laser due to the capability for high heat accumulation during nanoseconds as compared to picoseconds. The GO fabricated from Kapton® polymers with infrared laser irradiation also demonstrated a porous structure. The utility of these films in electrocatalysis has been verified[51-53]. We were able to achieve a low LOD of 7.15 nM in our study. To the best of our knowledge, the LOD for H_2O_2 sensing performed using LIG fabricated with a CO_2 laser has been in the mM range. Zhang et al.[53] reported the electrochemical performance of a Pt-decorated LIG electrode (Pt/LIG), a low-cost non-enzymatic sensor, which exhibited a detection limit of approximately 0.1 mM and a sensitivity of 248.4 mA $mM^{-1}cm^{-2}$. The LOD reported for carbon nanotube-modified laser-induced graphene was 0.5 mM[54]. Prussian blue-modified laser-induced graphene exhibited a LOD of 0.26 μmol L^{-1} [55]. Further, in our study we were able to obtain a correlation between the defect density and electron transfer kinetics in LIRGO films. Until now, very few studies have reported this relation for graphene films[56]. Our results will be important for further optimizing structure of graphene for advanced sensing. The LIRGO formed on Si in our study showed no degradation under 532 nm Raman measurement; hence, this robust sensor can be deployed in regions with intense radiation without the need for sophisticated packaging, enabling a cost-effective approach for advanced electrochemical sensing[10, 57]. To translate the findings of the experiment to commercial-scale repeatability of the experiments is important. The repeatability of samples was confirmed by performing repeated H_2O_2 sensing experiments with samples prepared after a span of two months. The a-C films deposited by pulsed laser deposition were thin and uniform hence, the initial laser pulse showed rGO formation with reproducible properties. The flatness of the laser annealed rGO films originates from the homogeneity in the melt front during regrowth. The Repeatability was confirmed until 10 pulses at 0.6 Jcm^{-2}. The comparison of typical sensitivity, linear response range, and the LOD values for rGO based H_2O_2 sensors reported in the literature and those obtained here are summarized in **Table 4**.

To understand the interference of other biomolecules within the potential window of H_2O_2 sensing, electrochemical sensing of was performed using a mixture containing 100 µM of uric acid, ascorbic acid, acetaminophen, dopamine, glucose, and ethanol along with H_2O_2 (**Fig 9 (a)**). A well-defined H_2O_2 reduction around -0.1 – -0.2 V (vs. Ag/AgCl) along with a gradual increase in signal upon rising the H_2O_2 concentration from 10 to 100 mM was observed. The results show that other analytes exhibit a separate broad signal and do not introduce any drift or changes in the H_2O_2 peak. Considering the requirement of the sensor to be flexible and easily wearable, we have further extended this study by fabricating rGO on flexible and optically transparent plastic substrates using laser-based processing. **Fig. 9(b, d)** shows the transparent and flexible nature of the plastic substrate on which rGO films were fabricated. **Fig. 9 (c)** shows the plastic substrate coated with a thin a-C layer. **Fig.9 (e)** demonstrates the laser-irradiated rGO formation on a strip of PE substrate. The attached video of graphene coated plastic substrates attached to hand serves as a proof of concept of applicability of our study for wearable sensing. The aspects such as strain to failure, and stretchability necessary to translate this fabricated product into real life application is a part of an ongoing study and will be reported elsewhere.

IV. Conclusions

This study offered a detailed insight into the diversity in electrochemical behavior of rGO thin films with major and minor structural modulations. The feasibility of electrochemical H_2O_2 sensing using a rGO working electrode fabricated by laser annealing route was verified. The best catalytic response towards electrochemical reduction was shown by LIRGO synthesized at 0.6 Jcm^{-2} with 10 pulses due to the presence of holes. A single pulse at laser annealing density (0.4 $Jcm^{-2} > E_d$) leads to surface melting of the a-C thin film and the formation of closed packed rGO with dangling bonds. The bonds act as active sites for the reduction of H_2O_2. However, the bulk still shows the presence of a-C, deteriorating the sensing activity. On the other hand, the LIRGO synthesized at a higher energy density (1 Jcm^{-2}) also exhibited poor sensing behavior due to the incorporation of a high amount of oxygen in the lattice, which is attributed to the high melt lifetime of molten carbon before solidification. The LIRGO synthesized at 0.6 Jcm^{-2} with 1 pulse showed a good response towards H_2O_2 sensing

due to the optimum amount of reduction and complete melting. However, after a single pulse at 0.6 Jcm^{-2}, the reduction takes place through the solid-state route. The deoxygenation resulted in a holey graphene structure with exposed edge planes. Here, the presence of dangling bonds due to reduction and at edge defects improved the limit of detection by several orders of magnitude (μM to nM). Further, we also demonstrated the successful implementation of rGO film fabrication on flexible plastic substrates, with excimer laser reduction opening up the possibility of flexible and cost-effective biosensors. The ability of laser irradiation to synthesize holey graphene structures with tunable hole size holds great potential for environmental applications, including the adsorption of toxic gases as well as environmental pollutants such as dyes and heavy metal ions.

V. Supporting Information

The supporting information includes experimental details, 2D and 3D AFM scans of LIRGO films, SEM images, CV curves for LIRGO film stability, fittings to the Raman spectra, I_d/I_g plots, as well as CV and calibration plots at different scan rates for the E_{10} LIRGO film and calculations.

VI. Acknowledgments

The authors would like to acknowledge NSF Award #1836767. We appreciate the help of Bella Ruiz (an undergraduate student) for assistance with the preparation of the schematic figure.

VII. References

(1) Wang, Q.; Lei, Y.; Wang, D.; Li, Y. Defect Engineering in Earth-Abundant Electrocatalysts for CO2 and N2 Reduction. *Energy Environ. Sci.* **2019**, *12* (6), 1730–1750. https://doi.org/10.1039/C8EE03781G.

(2) Wang, G.; Yu, M.; Feng, X. Carbon Materials for Ion-Intercalation Involved Rechargeable Battery Technologies. *Chem. Soc. Rev.* **2021**, *50* (4), 2388–2443. https://doi.org/10.1039/D0CS00187B.

(3) Joshi, P.; Riley, P. R.; Denning, W.; Shukla, S.; Khosla, N.; Narayan, J.; Narayan, R. Laser-Patterned Carbon Coatings on Flexible and Optically Transparent Plastic Substrates for Advanced Biomedical Sensing and Implant Applications. *J. Mater. Chem. C* **2022**. https://doi.org/10.1039/D1TC05176H.

(4) Arul, R.; Oosterbeek, R. N.; Robertson, J.; Xu, G.; Jin, J.; Simpson, M. C. The Mechanism of Direct Laser Writing of Graphene Features into Graphene Oxide Films Involves Photoreduction and Thermally

Assisted Structural Rearrangement. *Carbon N. Y.* **2016**, *99*, 423–431. https://doi.org/10.1016/J.CARBON.2015.12.038.

(5) Ghadim, E. E.; Rashidi, N.; Kimiagar, S.; Akhavan, O.; Manouchehri, F.; Ghaderi, E. Pulsed Laser Irradiation for Environment Friendly Reduction of Graphene Oxide Suspensions. *Appl. Surf. Sci.* **2014**, *301*, 183–188. https://doi.org/10.1016/j.apsusc.2014.02.036.

(6) Ye, R.; Chyan, Y.; Zhang, J.; Li, Y.; Han, X.; Kittrell, C.; Tour, J. M. Laser-Induced Graphene Formation on Wood. *Adv. Mater.* **2017**, *29* (37), 1702211. https://doi.org/10.1002/ADMA.201702211.

(7) Lin, J.; Peng, Z.; Liu, Y.; Ruiz-Zepeda, F.; Ye, R.; Samuel, E. L. G.; Yacaman, M. J.; Yakobson, B. I.; Tour, J. M. Laser-Induced Porous Graphene Films from Commercial Polymers. *Nat. Commun. 2014 51* **2014**, *5* (1), 1–8. https://doi.org/10.1038/ncomms6714.

(8) Narayan, J.; White, C. W.; Aziz, M. J.; Stritzker, B.; Walthuis, A. Pulsed Excimer (KrF) Laser Melting of Amorphous and Crystalline Silicon Layers. *J. Appl. Phys.* **1998**, *57* (2), 564. https://doi.org/10.1063/1.334738.

(9) Joshi, P.; Riley, P.; Gupta, S.; Narayan, R. J.; Narayan, J. Advances in Laser-Assisted Conversion of Polymeric and Graphitic Carbon into Nanodiamond Films. *Nanotechnology* **2021**, *32* (43), 432001. https://doi.org/10.1088/1361-6528/AC1097.

(10) Gupta, S.; Joshi, P.; Narayan, J. Electron Mobility Modulation in Graphene Oxide by Controlling Carbon Melt Lifetime. *Carbon N. Y.* **2020**, *170*, 327–337. https://doi.org/10.1016/j.carbon.2020.07.073.

(11) Zhang, Y.; Wan, Q.; Yang, N.; Zhang, Y.; Wan, Q.; Yang, N. Recent Advances of Porous Graphene: Synthesis, Functionalization, and Electrochemical Applications. *Small* **2019**, *15* (48), 1903780. https://doi.org/10.1002/SMLL.201903780.

(12) Zhang, C.; Jiang, H.; Ma, R.; Zhang, Y.; Chen, Q. Simple Non-Enzymatic Electrochemical Sensor for Hydrogen Peroxide Based on Nafion/Platinum Nanoparticles/Reduced Graphene Oxide Nanocomposite Modified Glassy Carbon Electrode. *Ionics (Kiel).* **2017**, *23* (5), 1309–1317. https://doi.org/10.1007/S11581-016-1944-2.

(13) Pizzino, G.; Irrera, N.; Cucinotta, M.; Pallio, G.; Mannino, F.; Arcoraci, V.; Squadrito, F.; Altavilla, D.; Bitto, A. Oxidative Stress: Harms and Benefits for Human Health. *Oxid. Med. Cell. Longev.* **2017**, *2017*. https://doi.org/10.1155/2017/8416763.

(14) Zheng, C.; Jin, X.; Li, Y.; Mei, J.; Sun, Y.; Xiao, M.; Zhang, H.; Zhang, Z.; Zhang, G. J. Sensitive Molybdenum Disulfide Based Field Effect Transistor Sensor for Real-Time Monitoring of Hydrogen Peroxide. *Sci. Reports 2019 91* **2019**, *9* (1), 1–9. https://doi.org/10.1038/s41598-018-36752-y.

(15) Sookhakian, M.; Zalnezhad, E.; Alias, Y. Layer-by-Layer Electrodeposited Nanowall-like Palladium-Reduced Graphene Oxide Film as a Highly-Sensitive Electrochemical Non-Enzymatic Sensor. *Sensors Actuators B Chem.* **2017**, *C* (241), 1–7. https://doi.org/10.1016/J.SNB.2016.10.053.

(16) Pournaghi-Azar, M. H.; Ahour, F. Electrochemical Reduction and Kinetics of Hydrogen Peroxide on the Rotating Disk Palladium-Plated Aluminum Electrode Modified by Prussian Blue Film as an Improved Electrocatalyst. *J. Solid State Electrochem.* **2010**, *14* (5), 823–828. https://doi.org/10.1007/S10008-009-0860-Z.

(17) Joshi, P.; Riley, P. R.; Mishra, R.; Machekposhti, S. A.; Narayan, R. Transdermal Polymeric Microneedle Sensing Platform for Fentanyl Detection in Biofluid. *Biosens. 2022, Vol. 12, Page 198* **2022**, *12* (4), 198. https://doi.org/10.3390/BIOS12040198.

(18) Neal, C. J.; Gupta, A.; Barkam, S.; Saraf, S.; Das, S.; Cho, H. J.; Seal, S. Picomolar Detection of Hydrogen Peroxide Using Enzyme-Free Inorganic Nanoparticle-Based Sensor. *Sci. Reports 2017 71* **2017**, *7* (1), 1–10. https://doi.org/10.1038/s41598-017-01356-5.

(19) Ebrahimi, A.; Zhang, K.; Dong, C.; Subramanian, S.; Butler, D.; Bolotsky, A.; Goodnight, L.; Cheng, Y.; Robinson, J. A. FeSx-Graphene Heterostructures: Nanofabrication-Compatible Catalysts for Ultra-Sensitive Electrochemical Detection of Hydrogen Peroxide. *Sensors Actuators, B Chem.* **2019**, *285*, 631–638. https://doi.org/10.1016/J.SNB.2018.12.033.

(20) Dinesh, B.; Mani, V.; Saraswathi, R, Direct Electrochemistry of Cytochrome c Immobilized on a Graphene Oxide–Carbon Nanotube Composite for Picomolar Detection of Hydrogen Peroxide.

https://doi.org/10.1039/C4RA02789B.

(21) Salimi, A.; Miranzadeh, L.; Hallaj, R.; Mamkhezri, H. Picomolar Detection of Hydrogen Peroxide at Glassy Carbon Electrode Modified with NAD+ and Single Walled Carbon Nanotubes. *Electroanalysis* **2008**, *20* (16), 1760–1768. https://doi.org/10.1002/ELAN.200804234.

(22) Mata, C. del R.; Moakhar, R.; Hosseini, I.; Nanoscale, M. J.-; 2021, A Nanostructured Microfluidic Device for Plasmon-Assisted Electrochemical Detection of Hydrogen Peroxide Released from Cancer Cells. *Nanoscale.* **2021**;13(34):14316-29.

(23) Narayan J. Laser annealing under the oxide layers in silicon. *Applied Physics Letters*. **1980**, 1; *37* (1), 66-8. https://doi.org/10.1063/1.91703.

(24) Tan, S. M.; Ambrosi, A.; Chua, C. K.; Pumera, M. Electron Transfer Properties of Chemically Reduced Graphene Materials with Different Oxygen Contents. *J. Mater. Chem. A* **2014**, *2* (27), 10668–10675. https://doi.org/10.1039/C4TA01034E.

(25) Yadav, R.; Joshi, P.; Hara, M.; Yana, T.; Hashimoto, S.; Yoshimura, M. Intercorrelation between Physical and Electrochemical Behavior of Nitrogen-Doping in Graphene for Symmetric Supercapacitor Electrode. *SN Appl. Sci.* **2020**, *2* (10). https://doi.org/10.1007/S42452-020-03401-X.

(26) Siddarth, R. K.; Manopriya, M.; Swathi, G.; Vijayvenkataraman, G.; Aranganayagam, K. R. One Step Synthesis of Reduced and Moringa Oleifera Treated Graphene Oxide: Characterization and Antibacterial Studies. **2019**, 54–62. https://doi.org/10.1007/978-3-030-25135-2_6.

(27) Sharma, R.; Chadha, N.; Saini, P. Determination of Defect Density, Crystallite Size and Number of Graphene Layers in Graphene Analogues Using X-Ray Diffraction and Raman Spectroscopy. *Indian J. Pure Appl. Phys.* **2017**, *55*, 625–629.

(28) Mathew, S.; Chan, T. K.; Zhan, D.; Gopinadhan, K.; Barman, A. R.; Breese, M. B. H.; Dhar, S.; Shen, Z. X.; Venkatesan, T.; Thong, J. T. L. The Effect of Layer Number and Substrate on the Stability of Graphene under MeV Proton Beam Irradiation. *Carbon N. Y.* **2011**, *49* (5), 1720–1726. https://doi.org/10.1016/J.CARBON.2010.12.057.

(29) Eckmann, A.; Felten, A.; Mishchenko, A.; Britnell, L.; Krupke, R.; Novoselov, K. S.; Casiraghi, C. Probing the Nature of Defects in Graphene by Raman Spectroscopy. *Nano Lett.* **2012**, *12* (8), 3925–3930. https://doi.org/10.1021/NL300901A/SUPPL_FILE/NL300901A_SI_001.PDF.

(30) Shin, J. K.; Lee, C. S.; Lee, K. R.; Eun, K. Y. Effect of Residual Stress on the Raman-Spectrum Analysis of Tetrahedral Amorphous Carbon Films. *Appl. Phys. Lett.* **2001**, *78* (5), 631–633. https://doi.org/10.1063/1.1343840.

(31) Stankovich, S.; Dikin, D. A.; Piner, R. D.; Kohlhaas, K. A.; Kleinhammes, A.; Jia, Y.; Wu, Y.; Nguyen, S. B. T.; Ruoff, R. S. Synthesis of Graphene-Based Nanosheets via Chemical Reduction of Exfoliated Graphite Oxide. *Carbon N. Y.* **2007**, *45* (7), 1558–1565. https://doi.org/10.1016/J.CARBON.2007.02.034.

(32) Canc, L. G.; Jorio, † A; Ferreira, E. H. M.; Stavale, F.; Achete, C. A.; Capaz, R. B.; Moutinho, M. V. O.; Lombardo, A.; Kulmala, T. S.; Ferrari, A. C. Quantifying Defects in Graphene via Raman Spectroscopy at Different Excitation Energies. *Nano Lett* **2011**, *11*, 3190–3196. https://doi.org/10.1021/nl201432g.

(33) Ferrari, A. C. Raman Spectroscopy of Graphene and Graphite: Disorder, Electron–Phonon Coupling, Doping and Nonadiabatic Effects. *Solid State Commun.* **2007**, *143* (1–2), 47–57. https://doi.org/10.1016/J.SSC.2007.03.052.

(34) Alsharaeh, E.; Ahmed, F.; Aldawsari, Y.; Khasawneh, M.; Abuhimd, H.; Alshahrani, M. Novel Synthesis of Holey Reduced Graphene Oxide (HRGO) by Microwave Irradiation Method for Anode in Lithium-Ion Batteries. *Sci. Reports 2016 61* **2016**, *6* (1), 1–13. https://doi.org/10.1038/srep29854.

(35) Chen, W.; Ge, C.; Li, J. T.; Beckham, J. L.; Yuan, Z.; Wyss, K. M.; Advincula, P. A.; Eddy, L.; Kittrell, C.; Chen, J.; Luong, D. X.; Carter, R. A.; Tour, J. M. Heteroatom-Doped Flash Graphene. *ACS Nano* **2022**.

(36) Kovtun, A.; Jones, D.; Dell'Elce, S.; Treossi, E.; Liscio, A.; Palermo, V. Accurate Chemical Analysis of Oxygenated Graphene-Based Materials Using X-Ray Photoelectron Spectroscopy. *Carbon N. Y.* **2019**, *143*, 268–275. https://doi.org/10.1016/J.CARBON.2018.11.012.

(37) Warner, J. H.; Fan, Y.; Robertson, A. W.; He, K.; Yoon, E.; Lee, G. Do. Rippling Graphene at the Nanoscale through Dislocation Addition. *Nano Lett.* **2013**, *13* (10), 4937–4944.

(38) Bachmatiuk, A.; Zhao, J.; Gorantla, S. M.; Martinez, I. G. G.; Wiedermann, J.; Lee, C.; Eckert, J.; Rummeli, M. H. Low Voltage Transmission Electron Microscopy of Graphene. *Small* **2015**, *11* (5), 515–542. https://doi.org/10.1002/SMLL.201401804.

(39) Joshi, P.; Haque, A.; Gupta, S.; Narayan, R. J.; Narayan, J. Synthesis of Multifunctional Microdiamonds on Stainless Steel Substrates by Chemical Vapor Deposition. *Carbon N. Y.* **2021**, *171*, 739–749. https://doi.org/10.1016/j.carbon.2020.09.064.

(40) Feng, H.; Cheng, R.; Zhao, X.; Duan, X.; Li, J. A Low-Temperature Method to Produce Highly Reduced Graphene Oxide. *Nat. Commun. 2013 41* **2013**, *4* (1), 1–8. https://doi.org/10.1038/ncomms2555.

(41) Barsoukov, E.; Macdonald, J. R. Impedance Spectroscopy: Theory, Experiment, and Applications. *Impedance Spectrosc. Theory, Exp. Appl.* **2005**, 1–595. https://doi.org/10.1002/0471716243.

(42) Affatato, S.; Bersaglia, G.; Rocchi, M.; Taddei, P.; Fagnano, C.; Toni, A. Wear Behaviour of Cross-Linked Polyethylene Assessed in Vitro under Severe Conditions. *Biomaterials* **2005**, *26* (16), 3259–3267. https://doi.org/10.1016/J.BIOMATERIALS.2004.07.070.

(43) Riley, P. R.; Joshi, P.; Penchev, H.; Narayan, J.; Narayan, R. J. One-Step Formation of Reduced Graphene Oxide from Insulating Polymers Induced by Laser Writing Method. *Cryst. 2021, Vol. 11, Page 1308* **2021**, *11* (11), 1308. https://doi.org/10.3390/CRYST11111308.

(44) De Lima, B. S.; Bernardi, M. I. B.; Mastelaro, V. R. Wavelength Effect of Ns-Pulsed Radiation on the Reduction of Graphene Oxide. **2019**. https://doi.org/10.1016/j.apsusc.2019.144808.

(45) Joshi, P.; Gupta, S.; Riley, P. R.; Narayan, R. J.; Narayan, J. Liquid Phase Regrowth of 〈110〉 Nanodiamond Film by UV Laser Annealing of PTFE to Generate Dense CVD Microdiamond Film. *Diam. Relat. Mater.* **2021**, 108481. https://doi.org/10.1016/j.diamond.2021.108481..

(46) Babar, N.; Joya, K, Spray-Coated Thin-Film Ni-Oxide Nanoflakes as Single Electrocatalysts for Oxygen Evolution and Hydrogen Generation from Water Splitting. *ACS Publ.* **2020**, *5* (19), 10641–10650.

https://doi.org/10.1021/acsomega.9b02960.

(47) Joya, K.; Ehsan, M.; Sohail, M., Nanoscale Palladium as a New Benchmark Electrocatalyst for Water Oxidation at Low Overpotential. *Journal of Materials Chemistry A*. **2019**, *7* (15) 9137-9144. https://doi.org/10.1039/C9TA01198F.

(48) Peng, Y. Y.; Liu, Y. M.; Chang, J. K.; Wu, C. H.; Ger, M. Der; Pu, N. W.; Chang, C. L. A Facile Approach to Produce Holey Graphene and Its Application in Supercapacitors. *Carbon N. Y.* **2015**, *C* (81), 347–356. https://doi.org/10.1016/J.CARBON.2014.09.067.

(49) Rajput, N. S.; Al Zadjali, S.; Gutierrez, M.; Esawi, A. M. K.; Al Teneiji, M. Synthesis of Holey Graphene for Advanced Nanotechnological Applications. **2021**. https://doi.org/10.1039/d1ra05157a.

(50) Lin, Z.; Ji, L.; Yan, T.; Xu, Y.; Sun, Z. Surface Defects State Analysis of Laser Induced Graphene from 4H-SiC. *J. Mater. Res. Technol.* **2020**, *9* (3), 5934–5941. https://doi.org/10.1016/J.JMRT.2020.03.120.

(51) Wang, F.; Mei, X.; Wang, K.; Dong, X.; Gao, M.; Zhai, Z.; Lv, J.; Zhu, C.; Duan, W.; Wang, W. Rapid and Low-Cost Laser Synthesis of Hierarchically Porous Graphene Materials as High-Performance Electrodes for Supercapacitors. https://doi.org/10.1007/s10853-018-03247-0.

(52) Idrees, M., Ahmed, S., Mohammed, Z., Korivi, N. S., & Rangari, V. 3D printed supercapacitor using porous carbon derived from packaging waste. Additive Manufacturing **2020**, 36, 101525.

(53) Zhang, Y.; Zhu, H.; Sun, P.; Sun, C. K.; Huang, H.; Guan, S.; Liu, H.; Zhang, H.; Zhang, C.; Qin, K. R. Laser-Induced Graphene-Based Non-Enzymatic Sensor for Detection of Hydrogen Peroxide. *Electroanalysis* **2019**, *31* (7), 1334–1341. https://doi.org/10.1002/ELAN.201900043.

(54) Settu, K., Lai, Y.C. and Liao, C.T.,. Carbon nanotube modified laser-induced graphene electrode for hydrogen peroxide sensing. *Materials Letters* **2021**, 300, p.130106.

(55) Matias, T.A., de Faria, L.V., Rocha, R.G., Silva, M.N., Nossol, E., Richter, E.M. and Muñoz, R.A., Prussian blue-modified laser-induced graphene platforms for detection of hydrogen peroxide. *Microchimica Acta* **2022**, 189(5), pp.1-9.

(56) Zhong, J.H., Zhang, J., Jin, X., Liu, J.Y., Li, Q., Li, M.H., Cai, W., Wu, D.Y., Zhan, D. and Ren, B..

Quantitative correlation between defect density and heterogeneous electron transfer rate of single layer graphene. *Journal of the American Chemical Society* **2014**, 136(47), pp.16609-16617.

(57) Shukla, S.; Joshi, P.; Riley, P.; Narayan, R. J. Square Wave Voltammetric Approach to Leptin Immunosensing and Optimisation of Driving Parameters with Chemometrics. *Biosens. Bioelectron*. **2022**. (Forthcoming)

(58) Das, S. R.; Nian, Q.; Cargill, A. A.; Hondred, J. A.; Ding, S.; Saei, M.; Cheng, G. J.; Claussen, J. C. 3D Nanostructured Inkjet Printed Graphene via UV-Pulsed Laser Irradiation Enables Paper-Based Electronics and Electrochemical Devices. *Nanoscale* **2016**, *8* (35), 15870–15879. https://doi.org/10.1039/C6NR04310K.

(59) Saraf, M.; Natarajan, K.; Mobin, S. M. Robust Nanocomposite of Nitrogen-Doped Reduced Graphene Oxide and MnO2 Nanorods for High-Performance Supercapacitors and Nonenzymatic Peroxide Sensors. *ACS Sustain. Chem. Eng.* **2018**, *6* (8), 10489–10504.

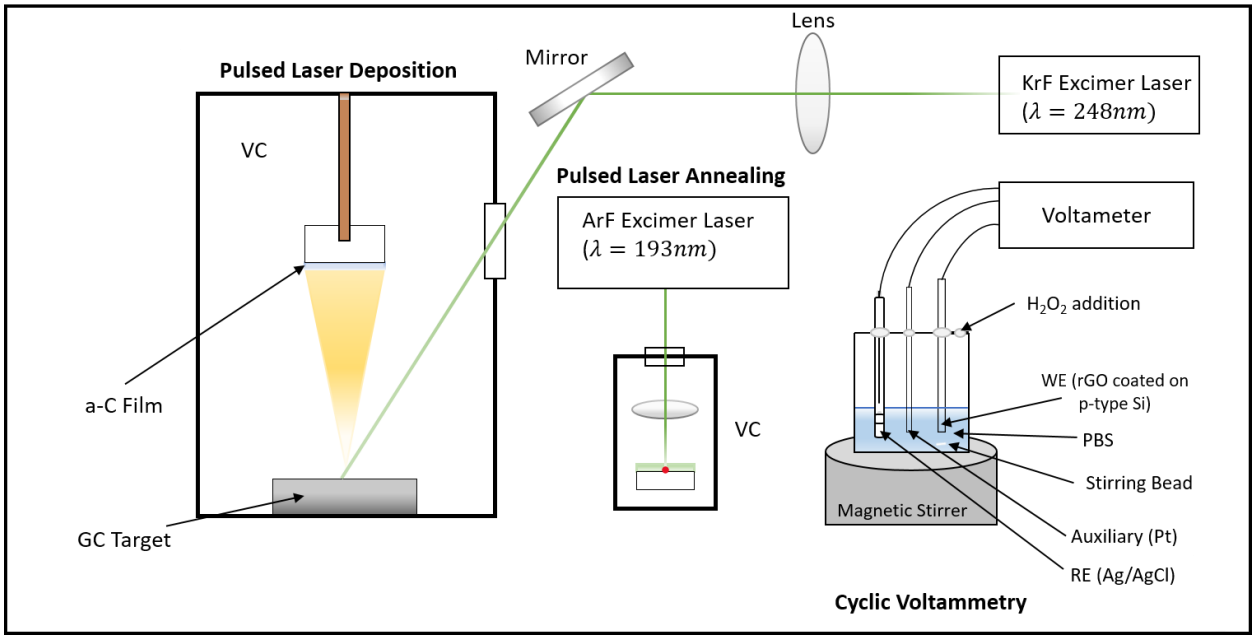

Fig. 1. Schematic illustration showing the synthesis of graphene-coated silicon working electrode for electrochemical hydrogen peroxide (H_2O_2) sensing, synthesized by depositing and irradiating amorphous carbon (a-C) thin films using an excimer laser inside a vacuum chamber (VC).

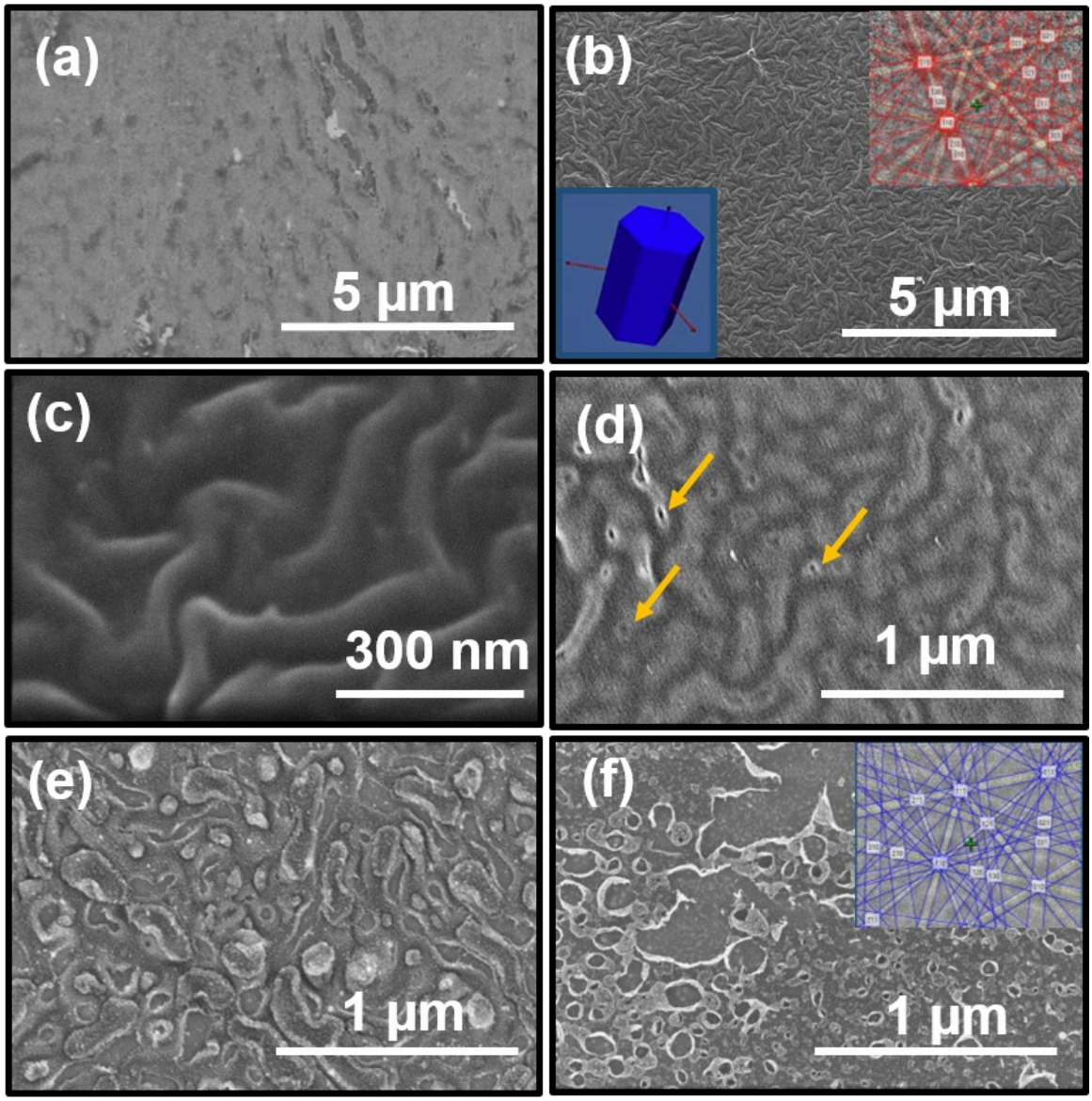

Fig. 2. SEM micrograph of a-C film after laser annealing at (a) 0.4 Jcm^{-2}, (b) 0.6 Jcm^{-2} with inset depicting the Kikuchi bands confirming the formation of crystalline graphene, (c) 0.6 Jcm^{-2} at high magnification to highlight the presence of ripple formation; SEM micrograph of a-C film after laser annealing at 0.6 Jcm^{-2} with (d) 5 pulses, (e) 10 pulses, (f) 15 pulses with inset depicting the Kikuchi bands from the <111> Si substrate.

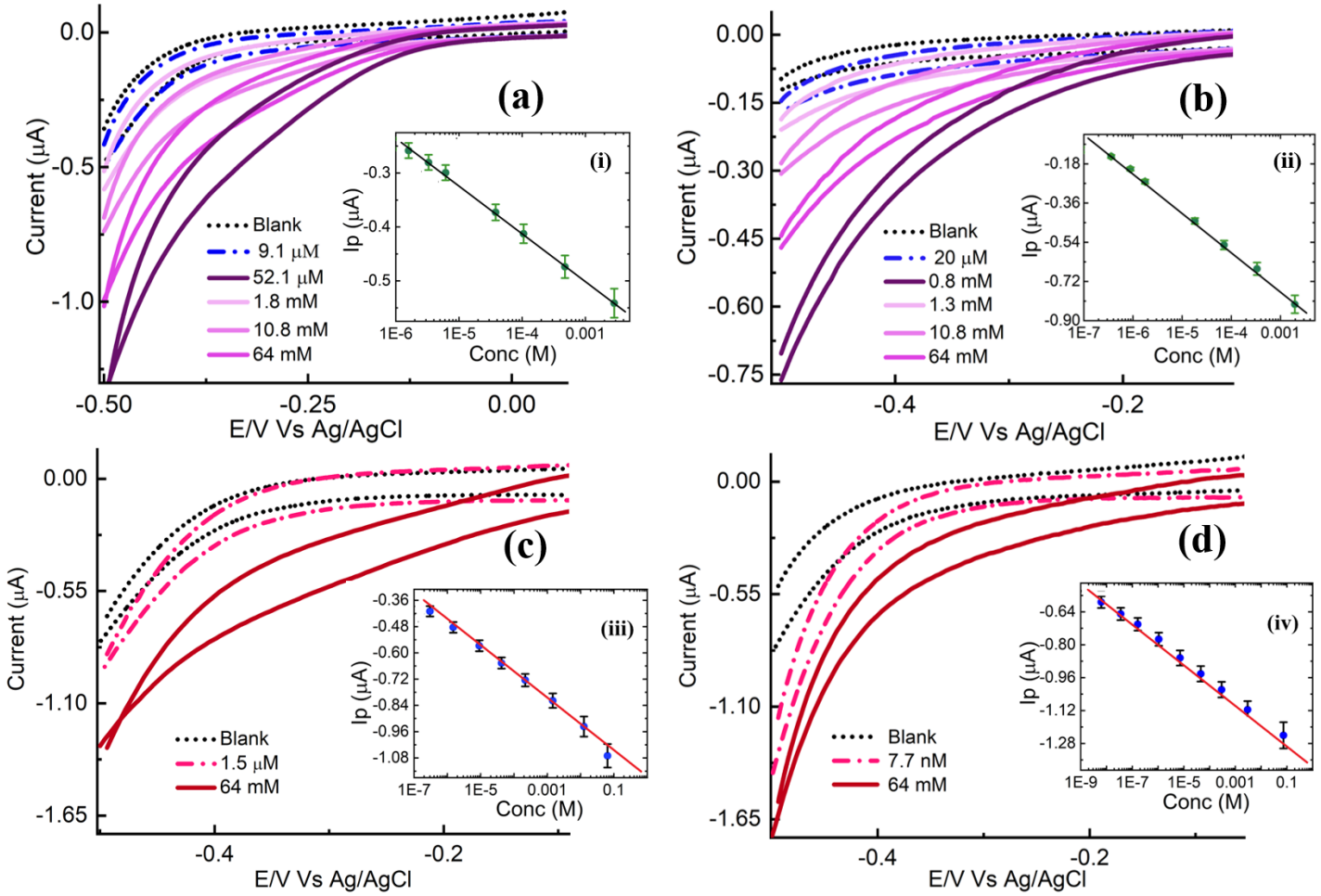

Fig. 3. CV curves for LIRGO electrodes (a) $E_{0.6}$, (b) $E_{1.0}$, (c) $E_{5\ pulses}$, and (d) $E_{10\ pulses}$. Inset pictures to the figures a – d, represent the corresponding calibration plots Ip vs Conc (i – iv).

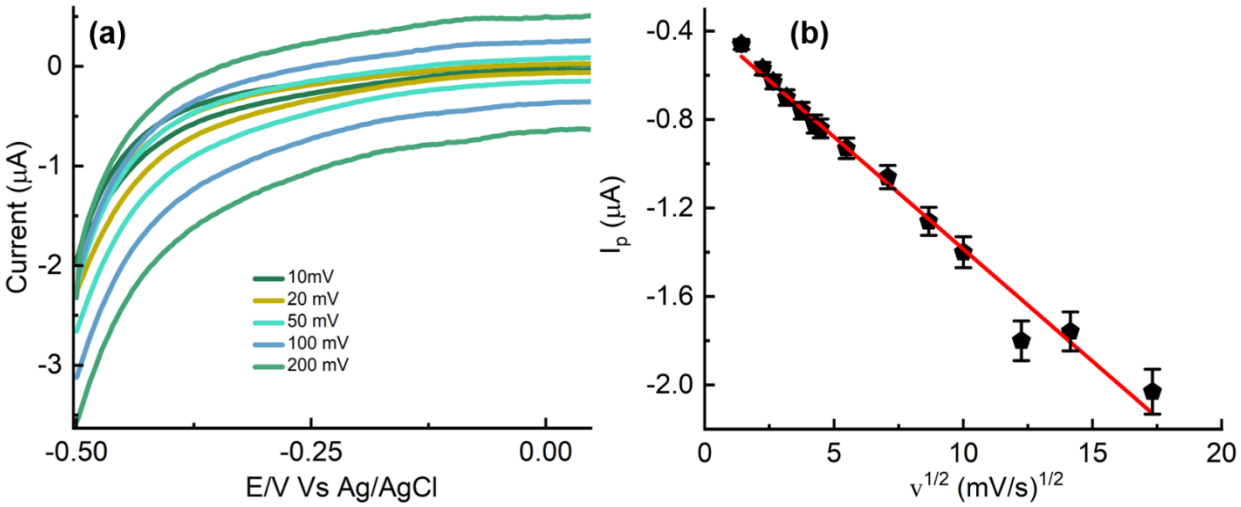

Fig. 4. (a) CV curves at different scan rates for $E_{10\ pulse}$, and (b) Scan rate vs i_p for $E_{10\ pulse}$.

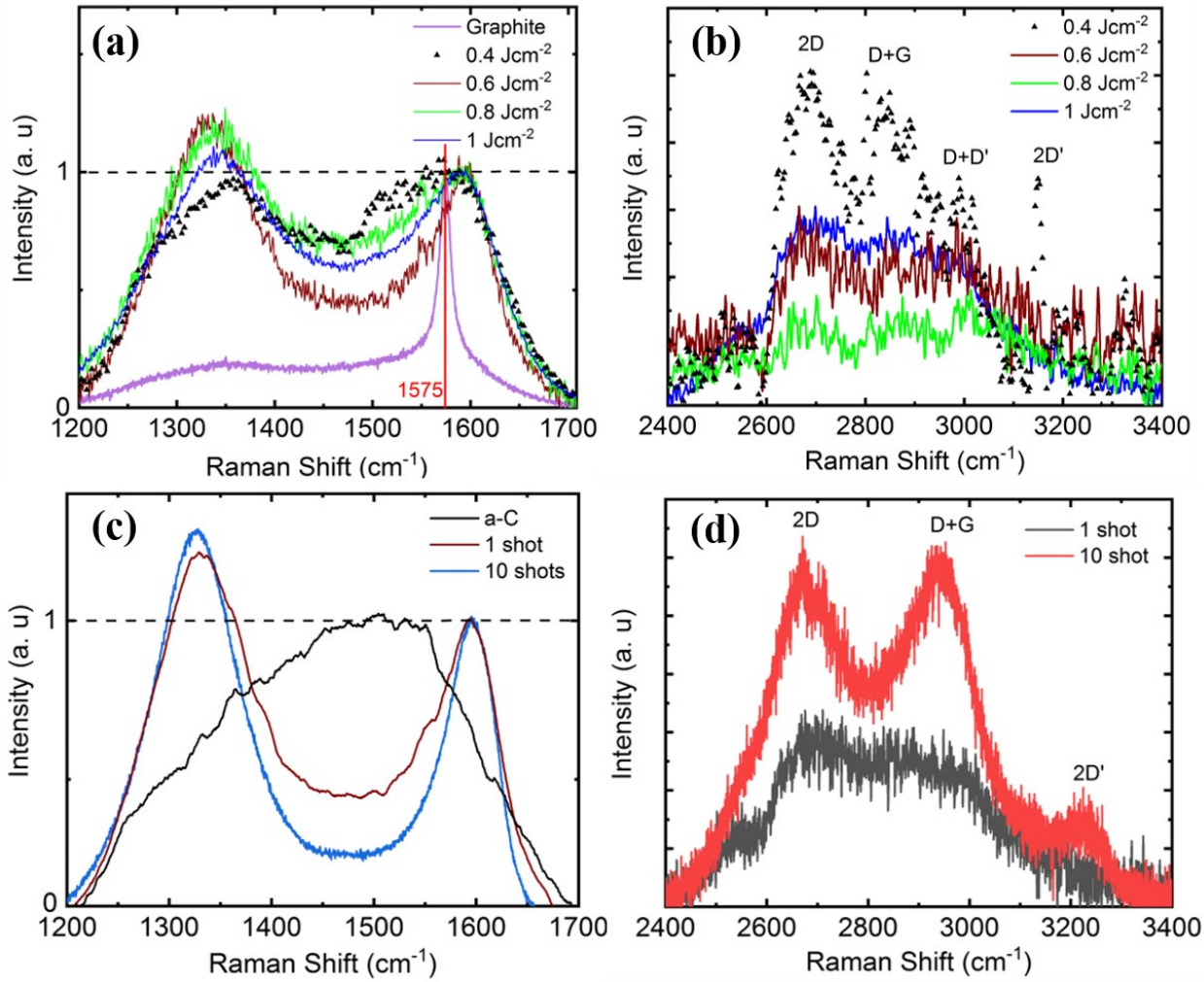

Fig. 5. (a, b) Raman spectrum of a-C and a-C after laser annealing at various energy densities, (c, d) Raman spectrum of unirradiated a-C and a-C laser irradiated with one and ten pulses at 0.6 Jcm^{-2}.

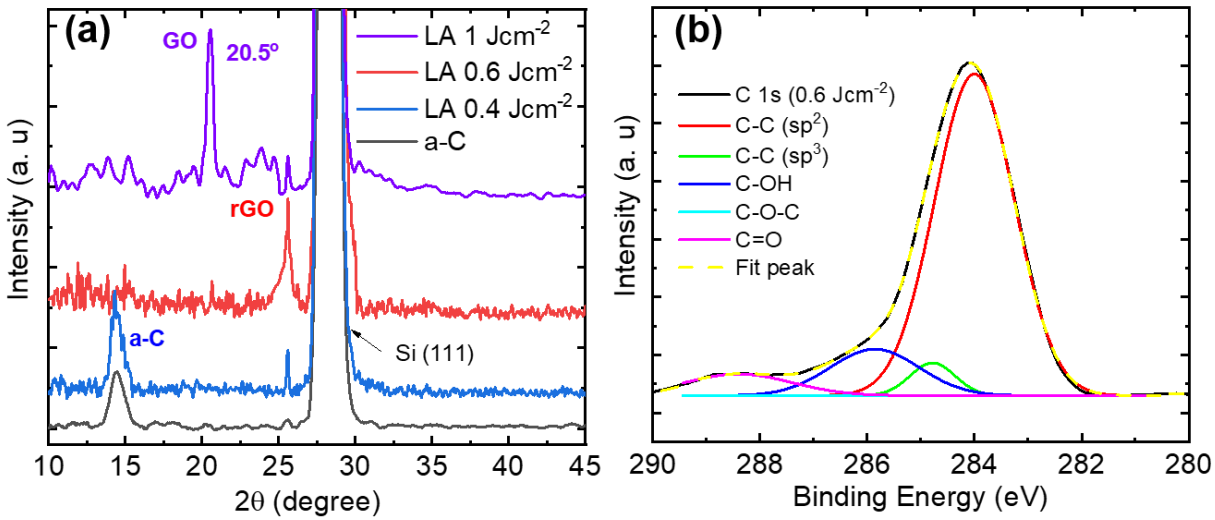

Fig. 6. (a) XRD results before and after laser annealing of a-C at different energy densities, and (b) XPS spectra of LIRGO synthesized at 0.6 Jcm^{-2}, indicating a minimum presence of oxygen in the structure after reduction.

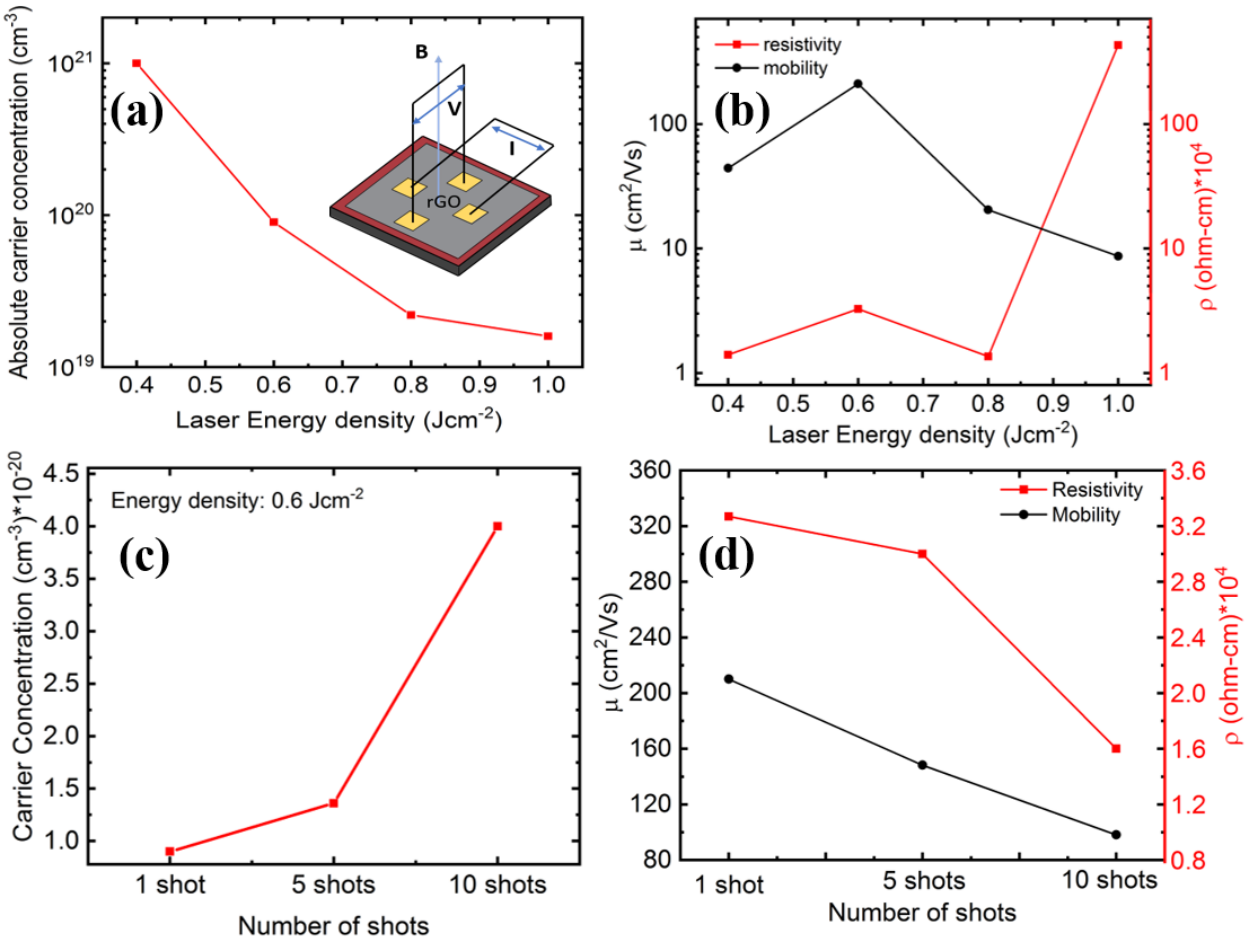

Fig. 7. (a) Resistivity and mobility of an a-C film as a function of laser annealing densities, (b) carrier concentration as a function of laser annealing densities, (c) carrier concentration as a function of # of pulses, and (d) resistivity and mobility of the a-C film as a function of # of pulses.

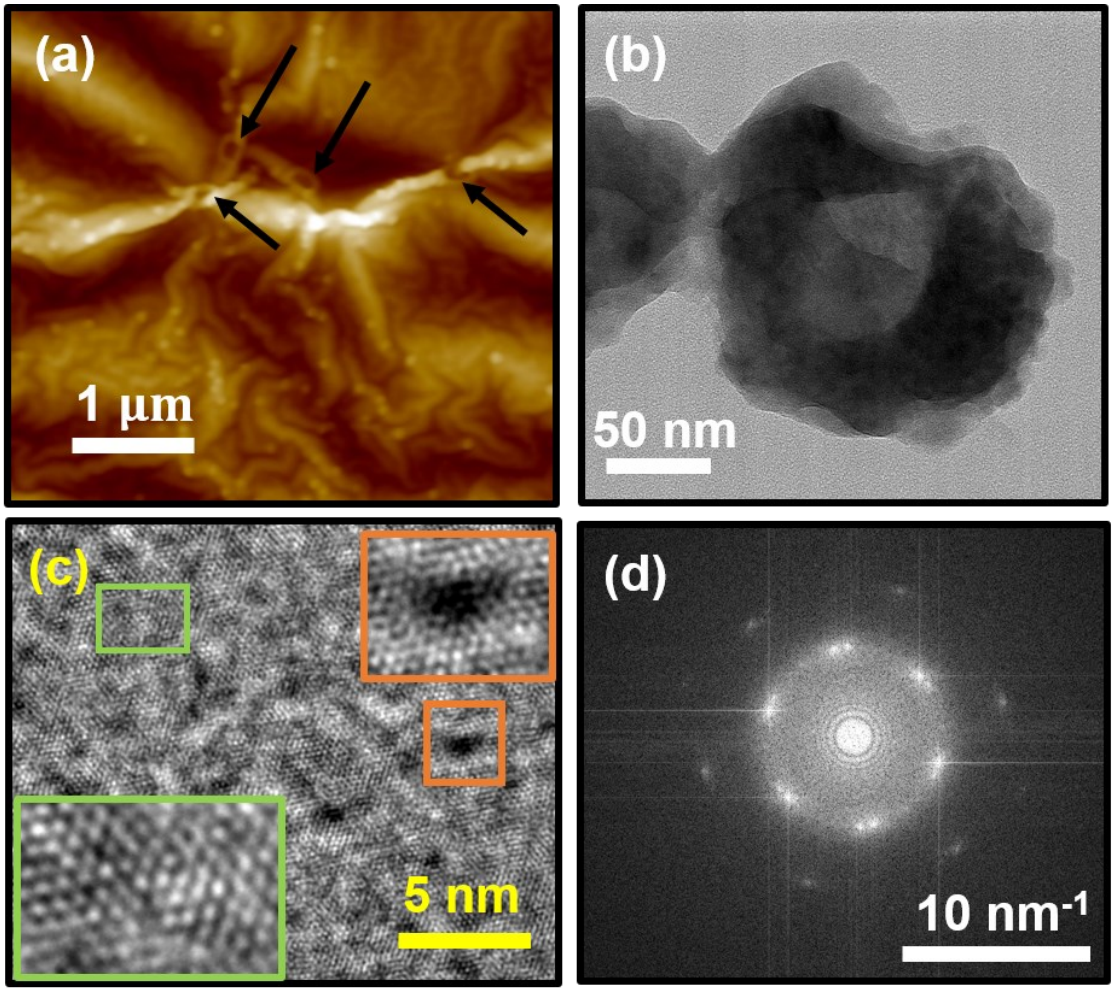

Fig. 8. (a) 2D AFM surface scan of LIRGO film irradiated at an energy density of 0.6 Jcm^{-2} (5 pulses), (b) TEM micrograph of rGO flake obtained by the drop cast method at 0.6 Jcm^{-2} (3 pulses), (c) HRTEM of LIRGO formed at 0.6 Jcm^{-2} (3 pulses) insets depicting the hexagonal network of atoms (green box) and nanoholes (orange box), and (d) FFT of (c).

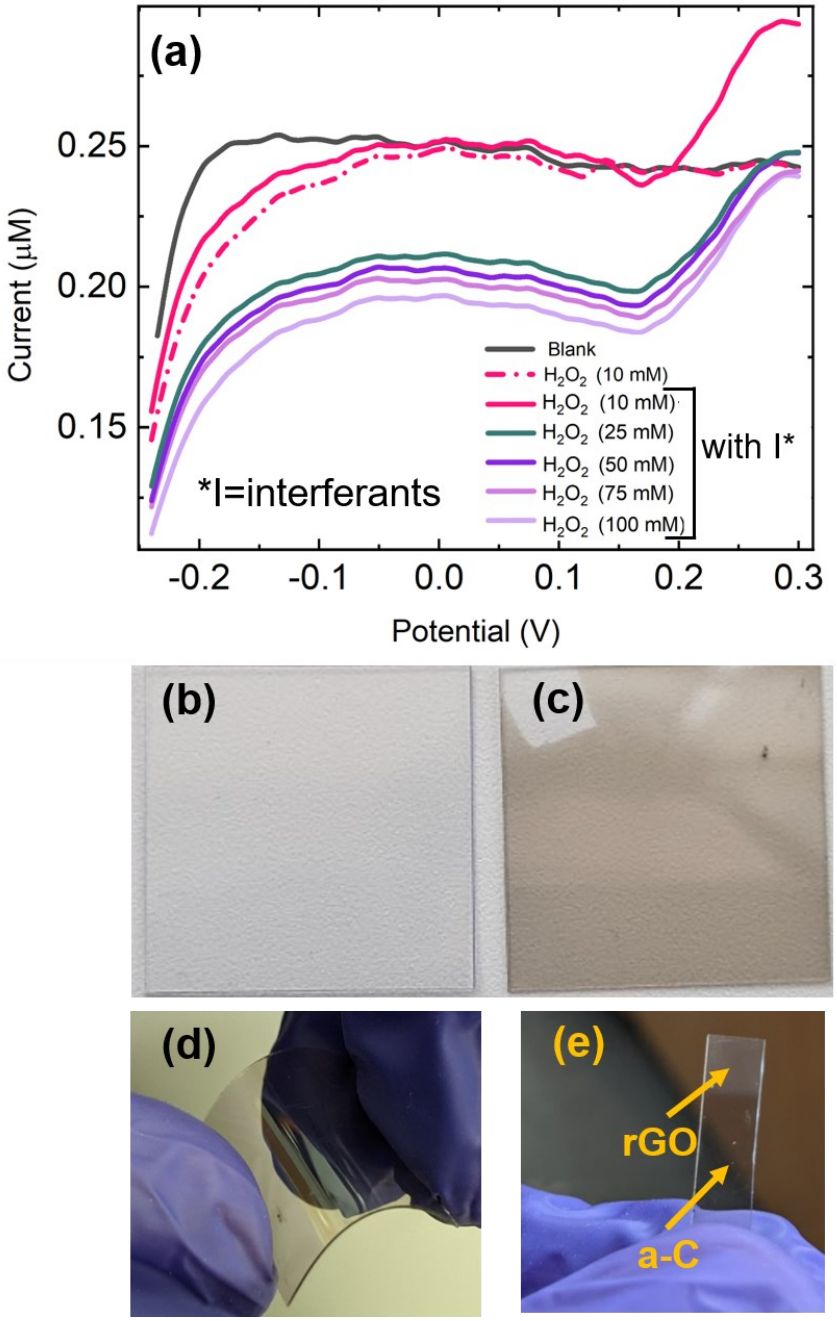

Fig. 9. (a) Square wave voltametric response of H_2O_2 (10 – 100 mM) in a mixture containing 100 μM (fixed concentration) of interfering analytes uric acid, ascorbic acid, acetaminophen, dopamine, glucose, and ethanol in PBS (0.1 M, pH 7.4). Images of optically transparent PE substrate: (b) uncoated and (c) coated with a thin a-C film. Images of: (d) coated polyethylene substrate subjected to flexing, and (e) a strip of PE showing the formation of LIRGO from a-C on the portion subjected to laser irradiation.

Table 1. Table summarizing the sensing properties of rGO as a function of energy density and the number of shots.

Laser Energy density (Jcm^{-2})	**# of pulses**	**LOD**	**Sensitivity ($\mu AmM^{-1}cm^{-2}$)**
0.4	1	~52.1mM	
0.6	1	25.4μM	0.1943
0.6	5	1.2μM	0.2024
0.6	10	7.15nM	0.2353
1	1	1.7 mM	0.1534

Table 2. Summary of information obtained from Raman spectra of rGO films.

Energy density (Jcm^{-2})	**I_d/I_g**	**L_a (nm)**	**# of defects (cm^{-2})**	**L_D (nm)**	**I_{2d}/I_g**
0.4	1.04	36.82	1.5645E+11	14.12177	0.34
0.6-1 pulse	2.5	15.32	3.76082E+11	9.108269	0.21
0.6-10 pulses	3.12	12.27	4.7E11	8.153208	0.4
0.8	2.1	NA			0.15
1	1.8	NA			0.22

Table 3. Table summarizing the electrical properties of rGO as a function of energy density and the number of shots.

Laser Energy density (Jcm^{-2})	**# of shots**	**Resistivity ($\Omega - cm$)**	**Mobility ($\frac{cm^2}{Vs}$)**
0.6	1	3.27E-4	210
	5	3E-4	148.2
	10	1.6E-4	98.16

Table 4. Comparison of PLA – rGO 2D films based electrochemical H_2O_2 sensor with other nanoscale sensors as reported in the literature.

Working electrode	**Reduction Potential (vs Ag/AgCl) V**	**Sensitivity**	**Concentration Range**	**LOD**	**Ref**
PLA-rGO film 0.6 Jcm^{-2} (10 pulses)	-0.09	0.235 μA/mM cm^{-2}	0.21 nM – 64 mM	7.15 nM	this work
PLA-rGO film 0.6 Jcm^{-2} (1 pulse)	-0.15	0.143 μA/mM cm^{-2}	0.21 nM – 64 mM	1.2 mM	this work
MoS_2/RGO FET	0.1	1 nA/pM cm^{-2}	1 pM to 100 nM	~ 1pM	[15]
Ceria nanoparticles (CNPs)	-0.4	0.156 μA/mM/cm^2	0.1 – 5 mM	0.1 pM	[18]
FeS_x/graphene	-0.5	–	10 – 100 mM	500 pM	[19]
Cyt *c*/GO–CNT	-0.2	0.533 μA pM^{-1} cm^{-2}	10 to 140 pM	27.7 pM	[20]
nanocavity/Gr	0.3	1520 μA mM^{-1} cm^{-2}	1 pM–10 μM	1 pM	[22]
3D graphene petals	0.8	3.32 μA/mM cm^{-2}	1 mM - 1 M	–	[58]
NRGO-MnO_2	0.1	2081 μA/mM cm^{-2}	0.4–121.2 μM	24 nM	[59]

Table Of Contents (TOC) graphic

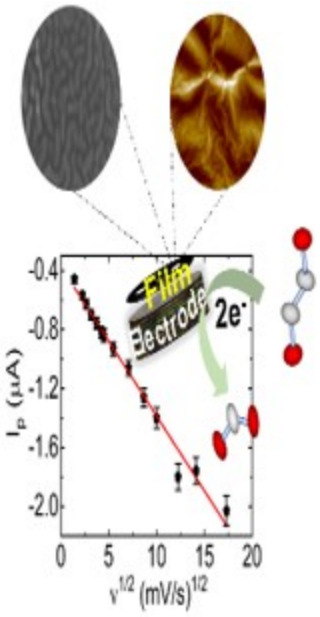
Film
Electrode
2e-
-0.4
-0.8
-1.2
-1.6
-2.0
I_p (μA)
0
5
10
15
20
$v^{1/2}$ (mV/s)$^{1/2}$